

See discussions, stats, and author profiles for this publication at: <https://www.researchgate.net/publication/372518860>

Modeling of firebrand dispersion and deposition in turbulent jet flows

Conference Paper · March 2023

CITATIONS

0

READS

125

3 authors, including:



[Aditya Mankame](#)

University of Alabama in Huntsville

7 PUBLICATIONS 12 CITATIONS

SEE PROFILE



[Babak Shotorban](#)

University of Alabama in Huntsville

96 PUBLICATIONS 1,207 CITATIONS

SEE PROFILE

13th U. S. National Combustion Meeting
Organized by the Central States Section of the Combustion Institute
March 19–22, 2023
College Station, Texas

Modeling of firebrand dispersion and deposition in turbulent jet flows

*Patrick Damiani , Aditya Mankame , and Babak Shotorban**

*Department of Mechanical and Aerospace Engineering, The University of Alabama in
Huntsville, Huntsville, AL 35899, USA*

**Corresponding author: babak.shotorban@uah.edu*

Abstract: Firebrands are critical in spreading fires by potentially causing secondary spot fires when dispersed by fire plumes and wind, and deposited into combustible materials. This paper is on the simulations of dispersion and deposition of firebrands by a round turbulent jet and their validation against the previous experimental data (Wadhvani et. al 2017). Firebrands were non-burning with cubiform and cylindrical shapes. Simulations were conducted by Fire Dynamic Simulator (FDS) with the large eddy simulation (LES) of turbulence representing the subgrid scales by the Modified Deardorff model and the particle Lagrangian tracking of dispersed firebrands. This took the translational motion into account but not the rotational motion for particles. First, simulations were performed without particles for free turbulent planar and round jets to validate the FDS flow solver in these configurations. For both jets, although the simulated mean velocities overall conformed to their respective self-similar profiles, the planer jet mean velocity displayed more consistency with these profiles. In both jets, the difference between the simulated Reynolds stresses and their previously measured values by others were within 30%. Then, simulations were preformed with firebrands in a computational configuration resembling the experimental firebrand generator setup of Wadhvani et. al (2017). Since the number of simulated firebrands was limited (210 particles), an accurate calculation of the landed firebrand distribution was not possible. However, the deposited cubiform firebrand pattern seemed to be more consistent with the previous experimental and simulation results than the deposited cylindrical firebrands. This may be attributed to the fact that the neglect of rotational motion was more critical to cylindrical firebrands.

Keywords: *firebrand deposition, turbulent jet flows, self-similarity analysis, large eddy simulation*

1. Introduction

The wildland urban interface (WUI) is the zone of transition between unoccupied land and human development, in which structures intermingle with undeveloped wildland fuels [1]. Wildfires throughout the WUI have resulted in immense property loss and the loss of human life. Between 2016 and 2022, there were seven wildfire disasters, in which each caused more than \$1B in damages, totalling \$91.9B and caused 255 fatalities [2]. Between 2020 and 2022, nearly 25M acres in the U.S. were consumed by fire, with approximately 7.5M acres in 2022 alone [3]. Five of the top–10 largest California wildfires were in 2020 [4]. The August Complex is the largest wildfire in California recorded history [4], burning 1,032,648 acres, destroying 935 structures, across seven counties between August 16th, 2020 to November 11th, 2020 [5]. The Dixie Fire, the second largest in California recorded history [4], burned 963,309 acres, destroying 1,311 structures, across five

counties between July 13th, 2021 to October 25th, 2021 [6]. The Office of Wildland Fire, working to combat U.S. wildfires, had a 2022 approved annual budget of \$1.53B and a 2023 requested annual budget of \$1.5B [7]. To help investigate wildfire challenges, experimental and numerical studies are conducted to provide knowledge and tools to improve policies, tactics, techniques, and procedures against wildfires.

Firebrands are lofted burning objects that can traverse short or long distances (sometimes several miles) and ignite recipient fuel after deposition. This mechanism plays a critical role in the spread of fires in wildlands and the WUI [8]. Firebrands most frequently have the form of tiny cylinders or discs [8]. Due to their airborne transport mechanism, firebrands can potentially circumvent firebreaks and other obstacles that would otherwise inhibit the spread of wildfires [8]. These discontinuous fires created by the deposition of firebrands are called spot fires. Spot fires pose a particular hazard in WUI areas where landscaping and buildings can become the recipient fuel for firebrands.

Various experimental and numerical research has been conducted for firebrand deposition. For example, the National Institute of Standards and Technology (NIST) Firebrand Generator (a.k.a. Dragon) is an apparatus used to experimentally study the role of firebrands in spread of fires [9]. It replicates wind-driven firebrand showers, depositing burning firebrands against various experimental samples, such as residential walls, roofs, and fences for the purpose of characterizing the risk to wildfire damage inherent to the materials and construction techniques [9–17]. Victoria University (VU), Australia, manufactured two apparatuses to characterize the pattern of the deposited firebrands. The VU firebrand generator prototype (VUFP) is a horizontally-oriented round turbulent jet capable of dispersing non-burning firebrands into an experimental area [18], and the VU Stainless Steel Generator (VUSSG) utilizes a similar jet capable of producing burning firebrands [19–21]. The VUFP was used in physical experiments to disperse non-burning cubiform and cylindrical firebrands with deposition results compared with simulated firebrand deposition results reported in Wadhwani et al. [18]. The model used to represent the flying motion of firebrands was found to have underpredicted the measured deposition results [18] for cylindrical firebrands. This model included the translational motion but neglected the rotational motion of firebrands.

Models that include both translational and rotational body dynamics of cylindrical particulate objects in a flow have been developed [22–26]. Translation is assumed to be under the influence of buoyancy, drag, and lift forces; and rotation is determined by the aerodynamic and air resistance torques. The model by Anand [25] and Mankame and Shotorban [26] also includes mass loss by pyrolysis and char oxidation, and the temperature loss is determined through pyrolysis, char oxidation, convection, and radiation. Anand [25] simulated firebrands released from a single point over a flat, open plane and showed the significance of flow turbulence dispersion and diffusion on the firebrand deposition. Mankame and Shotorban [26] simulated firebrands released in a wind flow to characterize the deposition on and around a solitary rectangular structure of various aspect ratios. It was observed that the rectangular structure formed a safe zone on the leeward side of the structure that was proportional to the cube height.

There is a need for a further validation of firebrand models. The current study is primarily driven by this and focuses on the validation of the particle models of Fire Dynamics Simulator (FDS) [27] versus the experimental and computational data of Wadhwani et al. [18]. The FDS particle models neglect the rotational motion. The VUFP apparatus from Wadhwani et al. [18] included a horizontally-oriented round turbulent jet that carried firebrands in air and deposited on the ground. Considering the significance of the flow in dynamics of particles, first, validation

studies were performed here for FDS to evaluate its performance in simulating free turbulent jets. Then, FDS v6.7.5 was used to simulate the VUFP experiments with firebrands and assess it against these experiments and their associated computations [18].

2. Mathematical Formulation

In this section, first, the self-similar solutions of the free turbulent jets, which are used for the assessment of the jet simulations, are shown. Then, the equations solved by FDS in the Lagrangian tracking of particles are shown. The equations solved for the flow by FDS are reported by McGrattan et al. [27].

2.1 Jet Flow Self-similarity Solutions

Planar and round turbulent jets have streamwise velocity profiles across the lateral extent that are self-similar in the far field region in excess of twenty jet diameters D (or widths W in the case of a planar jet) from the jet exit [28, 29].

One approach to determine the self-similar mean streamwise velocity profile is via the boundary layer equations for turbulent flows at a zero pressure gradient [30]. For a planar jet, the profile can be obtained [28–31] using

$$\frac{\bar{U}}{U_0} = \text{sech}^2(\sigma\eta), \quad (1)$$

where \bar{U} is the mean velocity, U_0 is the mean streamwise velocity at the centerline, i.e. $y = 0$, and $\eta = y/x$ is the dimensionless similarity variable. Here, x and y are the jet streamwise and cross-stream coordinates, respectively. Also, $\sigma = \alpha/S$ where $\alpha = \text{sech}^{-1}(1/\sqrt{2})$ and $S = y_{1/2}/x$ where S is defined as the spread rate of the jet with $y_{1/2}$ denoting the jet half-width. This is defined as the cross-stream coordinate of where $\bar{U} = U_0/2$. In turbulent jets, the spread rate S is constant in the region of self-similar as $y_{1/2} \propto x$. It is noted that $U_0 \propto x^{-1/2}$ for turbulent planar jets. Likewise, the velocity profile for the round jet turbulent flow is determined via the boundary layer theory [28–33]

$$\frac{\bar{U}}{U_0} = (1 + A\eta^2)^{-2}, \quad (2)$$

where $\eta = r/x$ is the dimensionless similarity variable and $A = (\sqrt{2} - 1)/S^2$, where x and r are the axial and radial coordinates, respectively, and $S = r_{1/2}/x$. For round jets, $r_{1/2} \propto x$ and $U_0 \propto x^{-1}$.

Another approach to determine self-similar profiles for turbulent jet flows is based on the gradient diffusion hypothesis [34], shown to conform more regularly to experimental results [33, 35–38]. This results in the following velocity profile for both planar and round jets

$$\frac{\bar{U}}{U_0} = e^{-(\eta/S)^2 \ln(2)}, \quad (3)$$

where the dimensionless similarity variable η and the spread rate S are consistent with their respective planar or round jet descriptions above.

2.2 Firebrand Equations

For the simulations configured for comparison to Wadhwani et al. [18], the non-burning cubiform and cylindrical firebrands were modeled with non-rotating spherical and cylindrical firebrands respectively. These firebrand models were included in FDS [27, 39] and were used in previous numerical work by Wadhwani et al. [18]. The spherical particle model was deemed appropriate for a cubiform firebrand because the cube sphericity $\psi = 0.806$ and uniform tumbling effects [19], and a cube has a similar drag coefficient to a sphere for particle Reynolds numbers < 100 [40]. The mean property values of firebrands reported by Wadhwani et al. [18] are used to configure the present numerical models. The spherical model was configured to match the cubiform firebrand mass and total wetted surface area. Equating the surface area of a sphere $SA_s = 4\pi(d_s/2)^2$ to the surface area of a cube $SA_c = 6l_c^2$, the diameter of the spherical model is

$$d_s = 2\sqrt{\left(\frac{3}{2\pi}\right)l_c}, \quad (4)$$

where l_c is the cubiform length. In order to match the cubiform mass m_c , the spherical model density is

$$\rho_s = \frac{3\rho_c l_c^3}{4\pi(d_s/2)^3}, \quad (5)$$

where ρ_c is the cubiform firebrand density. The cylindrical model was configured to match the cylindrical firebrand length l_{cy} , diameter d_{cy} , and mass m_{cy} .

The drag force of the fluid on a particle is

$$\vec{F}_D = C_d \vec{q} A, \quad (6)$$

where C_d is the drag coefficient, \vec{q} is the dynamic pressure of the fluid on the particle, and A is a cross-sectional area of the particle. The dynamic pressure is

$$\vec{q} = \frac{1}{2}\rho \left(\vec{U}_p - \vec{U} \right) |\vec{U}_p - \vec{U}|, \quad (7)$$

where ρ is the fluid density, \vec{U} is the fluid velocity, and \vec{U}_p is the particle velocity [27]. The cross-sectional areas for spherical and cylindrical models are

$$A_s = \pi \left(\frac{d_s}{2} \right)^2 \quad (8)$$

and

$$A_{cy} = d_{cy} l_{cy} \quad (9)$$

respectively [27]. The drag coefficients for the spherical and cylindrical models are calculated by

$$(\text{Sphere}) C_d = \begin{cases} 24/\text{Re}_d & \text{Re}_d < 1 \\ 24(0.85 + 0.15\text{Re}_d^{0.687})/\text{Re}_d & 1 \leq \text{Re}_d \leq 1000 \\ 0.44 & 1000 < \text{Re}_d \end{cases} \quad (10)$$

and

$$(\text{Cylinder}) C_d = \begin{cases} 10/\text{Re}_d^{0.8} & \text{Re}_d < 1 \\ 10(0.6 + 0.4\text{Re}_d^{0.8})/\text{Re}_d & 1 \leq \text{Re}_d \leq 1000 \\ 1 & 1000 < \text{Re}_d \end{cases} \quad (11)$$

respectively, in which the Reynolds number for the particle is

$$\text{Re}_d = \frac{|\vec{U}_p - \vec{U}|d_p}{\nu}, \quad (12)$$

where ν is the fluid kinematic viscosity. The particle acceleration is

$$\frac{d\vec{U}_p}{dt} = \vec{g} - \frac{\vec{F}_D}{m_p}, \quad (13)$$

where \vec{g} is the gravity vector and m_p is the particle mass. For the present work, planar jet and round jet simulations had $\vec{g} = 0 \text{ m/s}^2$, and the firebrand deposition simulations had $\vec{g} = (0, 0, -9.81) \text{ m/s}^2$. The particle position is $\vec{X}_p = \int \vec{U}_p dt$.

3. Computational Approach

FDS is an open-source computational fluid dynamic (CFD) fire-modeling code used to simulate fires through the integration of explicit-model incompressible flows in and around rigid objects, heat transfer in both fluids and solids, combustion processes, and the transport of particles [27]. The FDS v6.7.5 fluid dynamic and particle models were used for the present work. Fluid dynamics were computed using LES [41] with Modified Deardorff sub-grid scale turbulent model [42] and wall-adapting local eddy (WALE) near-wall turbulence model [43]. The core algorithm of FDS is an explicit predictor-corrector scheme that is second-order accurate in space and time [39]. It uses a rectilinear, staggered grid [44, 45] in which the geometry of stationary obstructions are interpolated to this underlying grid [27]. The Lagrangian particle model is two-way coupled, exchanging momentum between the fluid and the particles but not occupying any volume within Eulerian space [27].

4. Computational Setups

Three computational domains were created: one each for the planar jet and round jet simulations, and one domain for both firebrand deposition simulations. The planar jet simulation was a validation study compared to previous experimental and numerical work by Heskestad [46] and Yu et al. [38] respectively. The round jet simulation was a validation study compared to previous experimental work by Wygnanski and Fiedler [47]. The firebrand deposition simulations recreated previous experimental and numerical work by Wadhvani et al. [18]. The ambient air pressure was $p = 101,325 \text{ Pa}$, temperature was $T = 20^\circ\text{C}$, and density was $\rho = 1.195 \text{ kg/m}^3$. The dynamic and kinematic viscosities were $\mu = 1.8 \times 10^{-5} \text{ kg/m-s}$ and $\nu = 1.5063 \times 10^{-5} \text{ m}^2/\text{s}$ respectively. The following are details of the computational setups of each of these domains.

4.1 Planar Jet Simulation

A planar turbulent jet was simulated for comparison to previous experimental work by Heskestad [46] and previous numerical work by Yu et al. [38]. The planar jet slot was vertically-oriented with a width $W = 0.02$ m and a hydraulic diameter $D_H = 0.038$ m. Figure 1 shows the computational domain for the planar jet simulation with x , y , and z directions corresponding to the streamwise, cross-stream, and spanwise directions respectively. The domain consisted of two regions and was uniformly-discretized at $W/\Delta = 8$, which Yu et al. [38] concluded was an adequate resolution. Region 1 was designed to perform as the planar duct, spanning $-0.4 \leq x \leq 0$ m with a size of $0.4 \times 0.02 \times 0.4$ m. Region 2 was designed to support the jet flow, spanning $0 \leq x \leq 1$ m with a size of $1 \times 0.4 \times 0.4$ m. This domain had an extent of $50W$ in x and $\pm 10W$ in both y and z . For Region 1, closed boundary conditions, being impenetrable and no-slip, were implemented in y , and periodic boundary conditions were implemented in z . The inlet had a prescribed flow of $U = 10$ m/s. For Region 2, open boundary conditions [27] were implemented in y , and periodic boundary conditions were implemented in z . The boundary adjacent to the duct exit was closed, and the outlet boundary condition was open. Gravity was neglected, and the total simulation time was 10 s. Mean values were computed after the turbulence reached a statistically-stationary state, which was achieved by $t = 1.5$ s.

In this simulation, the mean centerline streamwise velocity at the jet exit was $U_j = 11.13$ m/s, and the mean streamwise velocity across the jet exit was $U_b = 9.797$ m/s. In previous experimental work by Heskestad [46], the Reynolds number presented was in the form $Re_W = U_j W \nu^{-1}$ with a value of 34,000, and the equivalent Reynolds number for the present work was 14,778. In previous numerical work by Yu et al. [38], the Reynolds number presented was in the form $Re_{D_H} = U_b D_H \nu^{-1}$ with a value of 26,927, and the equivalent Reynolds number for the present work was 24,715. It is noted that the self-similarity results should be independent of Reynolds number for turbulent jets with Reynolds numbers over 10,000 [28].

4.2 Round Jet Simulation

A round turbulent jet was simulated for comparison to previous experimental work by Wygnanski and Fiedler [47]. The horizontal round jet had an inside diameter of $D = 0.128$ m. Figure 5 shows the computational domain for the round jet simulation with x corresponding to the streamwise direction, and y and z are both cross-stream directions. The domain was not uniformly-discretized, consisting of four regions with grid resolutions $D/\Delta = 8, 8, 4$, & 2 for Regions 1, 2, 3, and 4 respectively. Region 1 was designed to support the round pipe, spanning $-5.12 \leq x \leq 0$ m with a size of $5.12 \times 0.64 \times 0.64$ m. Region 2 was designed to support the core flow, spanning $0 \leq x \leq 10.24$ m with a size of $10.24 \times 1.28 \times 1.28$ m. Region 3 was an annulus surrounding Region 2, spanning $0 \leq x \leq 10.24$ m creating a composite size of $10.24 \times 3.84 \times 3.84$ m. Region 4 was an additional annulus surrounding Region 3, spanning $0 \leq x \leq 10.24$ m creating a composite size of $10.24 \times 6.4 \times 6.4$ m. This domain had an extent of $80D$ in x and $\pm 25D$ in y and z . The open boundary condition was used for all external boundaries of the computational domain. Gravity was neglected, and the total simulation time was 120 s. Mean values were computed during statistically-stationary state, which was achieved by $t = 20$ s.

Considering Yu et al. [37]'s conclusion that ducts of appropriate length are necessary in FDS to ensure realistic turbulence at the jet exit, a step-wise rectilinear duct was used to approximate

a round pipe. This approximation was needed because FDS uses a structured grid. The external dimensions of the duct were $5.12 \times 0.192 \times 0.192$ m, and the internal dimensions were $5.088 \times 0.128 \times 0.128$ m at the y - and z -planes. The duct had a hydraulic diameter $D_H = 0.088$ m at the jet exit. A uniform flow of $U = 20.917$ m/s was prescribed to an area of size $0 \times 0.096 \times 0.096$ m at the beginning of the duct. The length of the duct interior was $L = 5.088$ m to ensure fully-developed turbulent flow at the jet exit [48]. From this implementation, the expected jet exit values were to be approximately: mean centerline streamwise velocity $U_0 = 20.078$ m/s, mean streamwise velocity across the jet exit $U_b = 17.114$ m/s, and Reynolds number $Re_{D_H} = U_b D_H \nu^{-1} = 99,982$ [48].

In this simulation, the mean centerline streamwise velocity at the jet exit was $U_j = 19.735$ m/s (1.7% from expected), and the mean streamwise velocity across the jet exit was $U_b = 16.862$ m/s (1.5% from expected). In previous experimental work by Wygnanski and Fiedler [47], the Reynolds number presented was in the form $Re_{D_H} = U_b D_H \nu^{-1}$ with a value of 100,000, and the equivalent Reynolds number for the present work was 98,510 (1.5% from expected).

4.3 Firebrand Deposition Simulations

A computational configuration was setup to simulate the VUFP firebrand generator presented in Wadhvani et al. [18]. This domain included a round turbulent jet, firebrands, and an experimental area with floor to accommodate firebrand deposition. The horizontal round jet had an inside diameter of $D = 0.1$ m. Figure 9 shows the computational domain for the firebrand deposition simulations with x corresponding to the streamwise direction, and y and z are both cross-stream directions. The domain was not uniformly-discretized and consisted of three regions with grid resolutions $D/\Delta = 10, 10, \& 5$ for Regions 1, 2, and 3 respectively. Region 1 was designed to support the VUFP, spanning $-4 \leq x \leq 0$ m with a size of $4 \times 0.2 \times 0.2$ m. Region 2 was designed to support the experimental area, spanning $0 \leq x \leq 0.5$ m with a size of $0.5 \times 1.2 \times 2$ m. Region 3 was designed to expand the experimental area, spanning $0.5 \leq x \leq 7.5$ m with a size $7 \times 1.2 \times 2$ m creating a composite size of $7.5 \times 1.2 \times 2$ m. This domain had an extent of $75D$ in x and ± 6 in y . The jet centerline height was $h = 0.96$ m which is $9.6D$ above the floor, and the domain had a vertical extent above the jet centerline of $10.4D$. The open boundary condition was used for all external boundaries of the computational domain except for the experimental area floor which had a closed boundary condition. The total simulation time was 40 s, and mean values were computed during statistically-stationary state, which was achieved by $t = 20$ s.

A step-wise rectilinear duct was used to approximate the VUFP. The external dimensions of the duct were $4 \times 0.128 \times 0.128$ m, and the internal dimensions were $3.99 \times 0.1 \times 0.1$ m at the y - and z -planes. The duct had a hydraulic diameter $D_H = 0.078$ m at the jet exit. A uniform flow of $U = 48.38$ m/s was prescribed to an area of size $0 \times 0.064 \times 0.064$ m at the beginning of the duct. The length of the duct interior was $L = 3.99$ m to ensure fully-developed turbulent flow at the jet exit [48]. From Wadhvani et al. [18], the reported mean centerline streamwise velocity at the jet exit was $U_0 = 29.5$ m/s. Computed from published velocity profile figures [18], the mean streamwise velocity across the jet exit was $U_b = 27.782$ m/s, and the Reynolds number was $Re_{D_H} = 184,439$.

For the cubiform firebrand deposition simulation, the mean centerline streamwise velocity at the jet exit was $U_j = 29.56$ m/s (0.2% from the VUFP), the mean streamwise velocity across the jet exit was $U_b = 23.561$ m/s (15.2% from the VUFP), and the Reynolds number was $Re_{D_H} = 122,474$ (33.6% from the VUFP). For the cylindrical firebrand deposition simulation, the mean

centerline streamwise velocity at the jet exit was $U_j = 29.525$ m/s (0.1% from the VUFP), the mean streamwise velocity across the jet exit was $U_b = 23.542$ m/s (15.3% from the VUFP), and the Reynolds number was $Re_{D_H} = 122,375$ (33.6% from the VUFP).

Wadhvani et al. [18] provided mean values for firebrand dimensions, and mean and standard deviations the densities and recorded velocities at the jet exit plane. For the present work, only the reported mean firebrand density and the mean streamwise velocity at the jet exit are used. For both simulations, 210 firebrands were introduced between $20 \leq t \leq 30$ s, with a random initial position within a $0 \times 0.064 \times 0.064$ m area centered on the jet exit. For the cubiform firebrand deposition simulation, the firebrands were represented with a spherical model whose diameter was $d = 0.0172$ m using eq. (4), density was $\rho = 309.9$ kg/m³ using eq. (5), and initial velocity was $\vec{U} = (12.5, 0, 0)$ m/s. For the cylindrical firebrand deposition simulation, the cylindrical model length was $l = 0.0116$ m, diameter was $d = 0.0062$ m, density was $\rho = 492.9$ kg/m³, and initial velocity was $\vec{U} = (13.4, 0, 0)$ m/s.

5. Results and Discussion

5.1 Planar Jet Simulation Results

Self-similarity analysis was performed on data within the range $20 \leq x/W \leq 40$. Figure 2(a) shows the planar jet mean centerline streamwise velocity U_0 normalized by the mean centerline streamwise velocity at the jet exit U_j plotted against x/W . A curve fit was applied to the reciprocal of this normalized velocity U_j/U_0 and is displayed in fig. 2(a). From this fit, the mean centerline streamwise velocity, dependent on x , is $U_0 = 11.13/(0.5303(x/W)^{1/2} - 0.404)$ m/s for U_0 within the range $20 \leq x/W \leq 40$. Figure 2(b) shows scatter data of the planar jet half-widths $y_{1/2}$ normalized by the jet width W plotted against x/W . This relationship is linear in the region of self-similarity [28, 33], and a linear curve fit is displayed in fig. 2(b). From this fit, the jet half-width, dependent on the streamwise position x , is $y_{1/2} = 0.1071(x/W) - 0.017$ m, and the slope of the line is the jet spread rate $S = 0.1071$.

Figure 3 shows the results for the planar jet mean streamwise velocities \bar{U} normalized by the mean centerline streamwise velocity U_0 plotted against η . This velocity profile is self-similar, and fig. 3 includes previous profiles obtained by Pope [28], Görtler [30], and Heskestad [46]. The curve Data (Present Work) is of mean values for \bar{U}/U_0 computed from the vector field at the central horizontal plane (i.e. $z = 0$) for nodes within the range $20 \leq x/W \leq 40$. The spread rate $S = 0.1071$ provides the coefficient $\sigma = \alpha/S = 8.231$ as shown in §2.1. The curve denoted Present Work A is the theoretical profile using eq. (1) which compared well with the equivalent theoretical curves [28, 30, 46]. The curve denoted Present Work C is the theoretical profile using eq. (3) which aligns well with the resulting mean \bar{U}/U_0 values throughout $0 \leq \eta \leq 0.25$.

Figure 4(a) shows the results for the planar jet mean Reynolds stresses in the streamwise direction $\overline{u'u'}$ normalized by the mean centerline streamwise velocity squared U_0^2 plotted against η . Figure 4(b) shows the results for the mean Reynolds stresses in the cross-stream directions $\overline{v'v'}$ normalized by the mean centerline streamwise velocity squared U_0^2 plotted against η . Figure 4(c) shows the results for the mean Reynolds shear stresses $\overline{u'v'}$ normalized by the mean centerline streamwise velocity squared U_0^2 plotted against η . According to Pope [28], for the planar jet, \bar{U}/U_0 and the Reynolds stress profiles become self-similar at $x/D \geq 40$ based on previous experimental work by Heskestad [46], Bradbury [49], and Gutmark and Wygnanski [50]. Figure 4 includes

previous experimental work by Heskestad [46] and previous numerical work by Yu et al. [38] for comparison. The resulting stress values compare well with previous numerical work by Yu et al. [38], and share $\overline{u'u'}/U_0^2$ underprediction, and $\overline{v'v'}/U_0^2$ and $\overline{u'v'}/U_0^2$ overprediction observations with Yu et al. [38] when compared against previous experimental work by Heskestad [46].

5.2 Round Jet Simulation Results

Self-similarity analysis was performed on data within the range $20 \leq x/D \leq 60$. Figure 6(a) shows the round jet mean centerline streamwise velocity U_0 normalized by the mean centerline streamwise velocity at the jet exit U_j plotted against x/D . The reciprocal of this normalized velocity U_j/U_0 is linear in the region of self-similarity [28, 33], and a linear curve fit is displayed in fig. 6(a). From this fit, the mean centerline streamwise velocity, dependent on x , is $U_0 = 19.735/(0.1976(x/D) - 0.403)$ m/s for U_0 within the range $20 \leq x/D \leq 60$. Figure 6(b) shows scatter data of the round jet half-widths $r_{1/2}$ normalized by the jet diameter D plotted against x/D . This relationship is linear in the region of self-similarity [28, 33], and a linear curve fit is displayed in fig. 6(b). From this fit, the jet half-width, dependent on the streamwise position x , is $r_{1/2} = 0.0892(x - 1.736 \times 10^{-1})$ m, and the slope of the line is the jet spread rate $S = 0.0892$.

Figure 7 shows the results for the round jet mean streamwise velocities \overline{U} normalized by the mean centerline streamwise velocity U_0 plotted against η . This velocity profile is self-similar, and fig. 7 includes previous profiles obtained by Pope [28], White [29], and Görtler [30]. The curve Data (Present Work) is of mean values for \overline{U}/U_0 computed from the vector field at the central horizontal plane (i.e. $z = 0$) and the central vertical plane (i.e. $y = 0$) for nodes within the range $20 \leq x/D \leq 60$. The spread rate $S = 0.0892$ provides the coefficient $A = (\sqrt{2} - 1)/S^2 = 52.00$ as shown in §2.1. The curve denoted Present Work B is the theoretical profile using eq. (2) which compares well with the equivalent theoretical curves [28–30]. The curve denoted Present Work C is the theoretical profile using eq. (3) which aligns well with the resulting mean \overline{U}/U_0 values throughout $0 \leq \eta \leq 0.25$.

Figure 8(a) shows the results for the round jet mean Reynolds stresses in the streamwise direction $\overline{u'u'}$ and normalized by the mean centerline streamwise velocity squared U_0^2 plotted against η . Figure 8(b) shows the results for the mean Reynolds stresses in the cross-stream directions $\overline{v'v'}$ normalized by the mean centerline streamwise velocity squared U_0^2 plotted against η . Figure 8(c) shows the results for the mean Reynolds shear stresses $\overline{u'v'}$ normalized by the mean centerline streamwise velocity squared U_0^2 plotted against η . These stress profiles are self-similar, and fig. 8 includes previous experimental work by Wygnanski and Fiedler [47]. The resulting stress values in the streamwise and cross-stream directions are underpredicted, and the shear stress values are overpredicted, when compared against previous experimental work by Wygnanski and Fiedler [47]. White [29] states that the turbulence components for a round jet do not become self-similar until at least $x/D = 50$, thus self-similarity might be observed using a larger domain.

5.3 Firebrand Deposition Simulation Results

For the non-burning cubiform firebrand simulation, the normalized mean streamwise velocity \overline{U}/U_0 profile at the jet exit is shown in fig. 10 with comparison against values replotted from figures provided by Wadhwani et al. [18]. The mean centerline streamwise velocity at the jet exit was $U_j = 29.560$ m/s which was well-matched to Wadhwani et al. [18] as designed, with only 0.2%

difference. The mean streamwise velocity across the jet exit was $U_b = 23.561$ m/s which deviated by 15.2% from that of the VUFP. The Reynolds number was $Re_{D_H} = 122,474$ which deviated by 33.6% from that of the VUFP.

For the non-burning cylindrical firebrand simulation, the mean centerline streamwise velocity at the jet exit was $U_j = 29.525$ m/s which again was well-matched to Wadhwani et al. [18] as designed, with only 0.1% difference. The mean streamwise velocity across the jet exit was $U_b = 23.542$ m/s deviated by 15.3% from that of the VUFP, and the Reynolds number was $Re_{D_H} = 122,375$ which deviated by 33.6% from that of the VUFP.

For the non-burning cubiform firebrand simulation, fig. 11(a) shows four sample trajectories of the non-rotating spherical firebrands from introduction into the simulation to deposition, along with the deposition for all firebrands. Figure 12(a) shows the firebrand depositions compared against the deposition distributions of both experimental and simulated non-burning cubiform firebrands replotted from figures provided by Wadhwani et al. [18]. The firebrands had a mean deposition location of $\bar{x} = 5.850$ m. The peak streamwise location of the experiential deposition distribution for the non-burning cubiform firebrands is at $x \approx 5.3$ m.

For the non-burning cylindrical firebrand simulation, fig. 11(b) shows four sample trajectories of the non-rotating cylindrical firebrands from introduction into the simulation to deposition, along with the deposition for all firebrands. Figure 12(b) shows the firebrand deposition compared against the deposition distributions of both experimental and simulated non-burning cylindrical firebrands replotted from figures provided by Wadhwani et al. [18]. The firebrands had a mean deposition location of $\bar{x} = 6.109$ m. The peak location of the experimental deposition distribution for the non-burning cylinder firebrands is at $x \approx 5.5$ m. The limited variation in firebrand initiation velocity is likely a dominant contributor to the over-precision of the resulting firebrand deposition pattern compared to the experimental and simulation deposition distributions presented in Wadhwani et al. [18]. Although both previous [18] and current numerical works uses FDS in simulations, there are differences in their generated particle deposition patterns, as evident in figure 12. A number of factors can attribute to these differences. It is uncertain whether all the configuration parameters in the present work conformed to any number of unpublished parameters previously used by Wadhwani et al. [18]. Self-similarity analysis provided insight into round jet flow expectations within FDS, which promoted various alterations to the domain configuration. Specifically, the present work uses a more uniform grid resolution in the firebrand deposition area and combines the round turbulent jet and the deposition area domains into one environment. The spherical particle model is configured to match the total wetted surface area of the cubiform firebrand, which is a departure from the configuration used by Wadhwani et al. [18]. Lastly, FDS v6.7.5 was used in the present work, while FDS v6.2.0 was used in previous work by Wadhwani et al. [18].

6. Summary and Conclusions

Self-similarity analysis was conducted on a planar and a round jet to evaluate the flow model used, and identify limitations and improvement opportunities. For the planar jet simulation, self-similarity results for the \bar{U}/U_0 profile were in agreement with previous experimental work by Heskestad [46] and previous numerical work by Yu et al. [38]. While the Reynolds stress profiles were consistent with previous numerical work by Yu et al. [38], the $\overline{u'u'}/U_0^2$ profile was underpre-

dicted, and the $\overline{v'v'}/U_0^2$ and $\overline{u'v'}/U_0^2$ profiles were overpredicted compared to previous experimental work by Heskestad [46]. For the round jet simulation, self-similarity results for the \overline{U}/U_0 profile were in agreement with theoretical velocity profiles by Pope [28], White [29], and Görtler [30], but the $\overline{u'u'}/U_0^2$ and $\overline{v'v'}/U_0^2$ profiles were underpredicted, and the $\overline{u'v'}/U_0^2$ profile was overpredicted compared to previous experimental work by Wygnanski and Fiedler [47].

For validation, it was important to establish a computational domain in which the performance improvements of the rotation-capable cylindrical firebrand model could be evaluated against the non-rotating equivalent model free from any potential contributing influences due to computational environmental differences between the present work and previous numerical work by Wadhwani et al. [18]. To this end, it was decided that the same particle models used in the previous numerical work were to be rerun in the present work within the validation domain. Firebrand simulations were conducted for non-burning cubiform and cylindrical firebrands dispersed from a round jet for the purpose of establishing baseline accuracy for future work. The round jet implemented did conform to the centerline streamwise velocity as designed, but did not accurately match the flow velocity profile observable in Wadhwani et al. [18]. Both the cubiform and cylindrical firebrand simulations resulted in a mean firebrand deposition location that had fair accuracy to previous experimental work by Wadhwani et al. [18], but the dispersion patterns were overly precise due to limited variation in initial conditions. Future work will include increased firebrand variation to improve dispersion accuracy by including more diverse particles based on the statistical variations in the previous experimental firebrand properties and velocities provided in Wadhwani et al. [18]. Additionally, future work will include firebrand deposition simulations of previous experimental work by Wadhwani [19] which includes non-burning and burning firebrand deposition results from a round turbulent jet. This baseline performance will be used in validation work for the cylindrical firebrand model that accounts for rotational body dynamics [24–26].

Acknowledgements

Acknowledgement is extended to Dr. R. Wadhwani for being available to answer questions about the Victoria University firebrand generators and previous models of these generators, FDS developer Dr. M. Vanella for HPC configuration technical support, all NIST developers for helpful guidance in the FDS online forums, and the Alabama Supercomputer Authority for high performance computing resources and technical support.

References

- [1] U.S. Fire Administration, *Wildfire and the Wildland Urban Interface (WUI)*, URL: <https://www.usfa.fema.gov/wui/>, (accessed: 2023-01-22).
- [2] National Centers of Environmental Information, *Billion-Dollar Weather and Climate Disasters*, URL: <https://www.ncei.noaa.gov/access/billions/>, (accessed: 2023-01-23).
- [3] National Centers of Environmental Information, *Annual 2022 Wildfires Report*, URL: <https://www.ncei.noaa.gov/access/monitoring/monthly-report/fire/202213>, (accessed: 2023-01-22).

- [4] California Department of Forestry and Fire Protection, *Top 20 Largest California Wildfires*, URL: https://www.fire.ca.gov/media/4jandlhh/top20_acres.pdf, (accessed: 2022-10-24).
- [5] California Department of Forestry and Fire Protection, *August Complex (includes Doe Fire) Incident*, URL: <https://www.fire.ca.gov/incidents/2020/8/16/august-complex-includes-doe-fire/>, (accessed: 2023-01-23).
- [6] California Department of Forestry and Fire Protection, *Dixie Fire Incident Report*, URL: <https://www.fire.ca.gov/incidents/2021/7/13/dixie-fire/>, (accessed: 2023-01-23).
- [7] U.S. Department of the Interior, *Office of Wildland Fire Budget*, URL: <https://www.doi.gov/wildlandfire/budget>, (accessed: 2023-01-23).
- [8] E. Koo, P. J. Pagni, D. R. Weise, and J. P. Woycheese, Firebrands and spotting ignition in large-scale fires, *International Journal of Wildland Fire* 19 (2010) 818–843.
- [9] S. L. Manzello, S. Suzuki, M. J. Gollner, and A. C. Fernandez-Pello, Role of firebrand combustion in large outdoor fire spread, *Progress in energy and combustion science* 76 (2020) 100801.
- [10] S. L. Manzello, S.-H. Park, S. Suzuki, J. R. Shields, and Y. Hayashi, Experimental investigation of structure vulnerabilities to firebrand showers, *Fire Safety Journal* 46 (2011) 568–578.
- [11] S. L. Manzello, S. Suzuki, and Y. Hayashi, Enabling the study of structure vulnerabilities to ignition from wind driven firebrand showers: A summary of experimental results, *Fire Safety Journal* 54 (2012) 181–196.
- [12] S. L. Manzello, S. Suzuki, and Y. Hayashi, Exposing siding treatments, walls fitted with eaves, and glazing assemblies to firebrand showers, *Fire Safety Journal* 50 (2012) 25–34.
- [13] S. L. Manzello, Enabling the investigation of structure vulnerabilities to wind-driven firebrand showers in wildland-urban interface (WUI) fires, *Fire Safety Science* 11 (2014) 83–96.
- [14] S. L. Manzello and S. Suzuki, Experimental investigation of wood decking assemblies exposed to firebrand showers, *Fire safety journal* 92 (2017) 122–131.
- [15] S. Manzello, S. Suzuki, and I. Hagiwara, Exposing Fencing Assemblies to Firebrand Showers Characteristic of Burning Structures, in, *Proceedings of the 2017 Fire and Materials Conference*, San Francisco, CA, US, (2017).
- [16] S. L. Manzello and S. Suzuki, Influence of board spacing on mitigating wood decking assembly ignition, *Fire safety journal* 110 (2019) 102913.
- [17] S. Suzuki and S. L. Manzello, Initial study on thatched roofing assembly ignition vulnerabilities to firebrand showers, *Fire safety journal* 103 (2019) 34–37.
- [18] R. Wadhvani, D. Sutherland, A. Ooi, K. Moinuddin, and G. Thorpe, Verification of a Lagrangian particle model for short-range firebrand transport, *Fire Safety Journal* 91 (2017) 776–783.

- [19] R. Wadhwani, Physics-based simulation of short-range spotting in wildfires, PhD thesis, Victoria University, 2019.
- [20] R. Wadhwani, C. Sullivan, A. Wickramasinghe, M. Kyng, N. Khan, and K. Moinuddin, A review of firebrand studies on generation and transport, *Fire safety journal* (2022) 103674.
- [21] R. Wadhwani, D. Sutherland, A. Ooi, and K. Moinuddin, Corrigendum to: Firebrand transport from a novel firebrand generator: numerical simulation of laboratory experiments, *International journal of wildland fire* 31 (2022) 649–649.
- [22] C. Yin, L. Rosendahl, S. K. Kær, and H. Sørensen, Modelling the motion of cylindrical particles in a nonuniform flow, *Chemical Engineering Science* 58 (2003) 3489–3498.
- [23] L. A. Oliveira, A. G. Lopes, B. R. Baliga, M. Almeida, and D. X. Viegas, Numerical prediction of size, mass, temperature and trajectory of cylindrical wind-driven firebrands, *International journal of wildland fire* 23 (2014) 698–708.
- [24] C. Anand, B. Shotorban, and S. Mahalingam, Dispersion and deposition of firebrands in a turbulent boundary layer, *International Journal of Multiphase Flow* 109 (2018) 98–113.
- [25] C. Anand, Computational investigations of ignition characteristics of live fuels and deposition of firebrands in a turbulent boundary layer, PhD thesis, The University of Alabama in Huntsville, 2018.
- [26] A. Mankame and B. Shotorban, Deposition Characteristics of Firebrands on and Around Rectangular Cubic Structures, *Frontiers in Mechanical Engineering* (2021) 53.
- [27] K. McGrattan, S. Hostikka, J. Floyd, R. McDermott, and M. Vanella, Fire Dynamics Simulator Technical Reference Guide Volume 1: Mathematical Model, NIST Special Publication - Sixth Edition Report No. 1018-1, U.S. Department of Commerce, National Institute of Standards and Technology, 2020.
- [28] S. Pope, *Turbulent Flows*, Cambridge University Press, 2000.
- [29] F. White, *Viscous Fluid Flow*, McGraw-Hill Education, 2006.
- [30] H. Görtler, Berechnung von Aufgaben der freien Turbulenz auf Grund eines neuen Näherungsansatzes, *J. Appl. Math. Mech, ZAMM* 22 (1942) 244–254.
- [31] B. Eisfeld, Characteristics of incompressible free shear flows and implications for turbulence modeling, *AIAA Journal* 59 (2021) 180–195.
- [32] H. Schlichting, Laminare Strahlenausbreitung, *Z. Angew. Math. Mech.* 13 (1933) 260–263.
- [33] T. Basset, B. Viggiano, T. Barois, M. Gibert, N. Mordant, R. B. Cal, R. Volk, and M. Bourgoïn, Entrainment, diffusion and effective compressibility in a self-similar turbulent jet, *arXiv preprint arXiv:2201.02443* (2022).
- [34] R. So and B. Hwang, On similarity solutions for turbulent and heated round jets, *Zeitschrift für angewandte Mathematik und Physik ZAMP* 37 (1986) 624–631.
- [35] G. Lipari and P. K. Stansby, Review of experimental data on incompressible turbulent round jets, *Flow, turbulence and combustion* 87 (2011) 79–114.
- [36] R. C. Deo, J. Mi, and G. J. Nathan, The influence of nozzle-exit geometric profile on statistical properties of a turbulent plane jet, *Experimental Thermal and Fluid Science* 32 (2007) 545–559.

- [37] L.-X. Yu, T. Beji, F. Liu, M.-C. Weng, and B. Merci, Analysis of FDS 6 simulation results for planar air curtain related flows from straight rectangular ducts, *Fire Technology* 54 (2018) 419–435.
- [38] L.-X. Yu, T. Beji, G. Maragkos, F. Liu, M.-C. Weng, and B. Merci, Assessment of numerical simulation capabilities of the fire dynamics simulator (FDS 6) for planar air curtain flows, *Fire technology* 54 (2018) 583–612.
- [39] K. McGrattan, S. Hostikka, J. Floyd, R. McDermott, and M. Vanella, *Fire Dynamics Simulator User’s Guide*, NIST Special Publication - Sixth Edition Report No. 1019, U.S. Department of Commerce, National Institute of Standards and Technology, 2020.
- [40] A. Haider and O. Levenspiel, Drag coefficient and terminal velocity of spherical and non-spherical particles, *Powder technology* 58 (1989) 63–70.
- [41] J. Smagorinsky, General circulation experiments with the primitive equations: I. The basic experiment, *Monthly weather review* 91 (1963) 99–164.
- [42] J. W. Deardorff, Stratocumulus-capped mixed layers derived from a three-dimensional model, *Boundary-Layer Meteorology* 18 (1980) 495–527.
- [43] F. Nicoud and F. Ducros, Subgrid-scale stress modelling based on the square of the velocity gradient tensor, *Flow, turbulence and Combustion* 62 (1999) 183–200.
- [44] F. H. Harlow and J. E. Welch, Numerical calculation of time-dependent viscous incompressible flow of fluid with free surface, *The physics of fluids* 8 (1965) 2182–2189.
- [45] Y. Morinishi, T. S. Lund, O. V. Vasilyev, and P. Moin, Fully conservative higher order finite difference schemes for incompressible flow, *Journal of computational physics* 143 (1998) 90–124.
- [46] G. Heskestad, Hot-wire measurements in a plane turbulent jet, *Journal of Applied Mechanics* 32 (1965) 721–734.
- [47] I. Wygnanski and H. Fiedler, Some measurements in the self-preserving jet, *Journal of Fluid Mechanics* 38 (1969) 577–612.
- [48] F. White, *Fluid Mechanics*, McGraw-Hill International Editions, WCB/McGraw-Hill, 1999.
- [49] L. Bradbury, The structure of a self-preserving turbulent plane jet, *Journal of Fluid Mechanics* 23 (1965) 31–64.
- [50] E. Gutmark and I. Wygnanski, The planar turbulent jet, *Journal of fluid Mechanics* 73 (1976) 465–495.

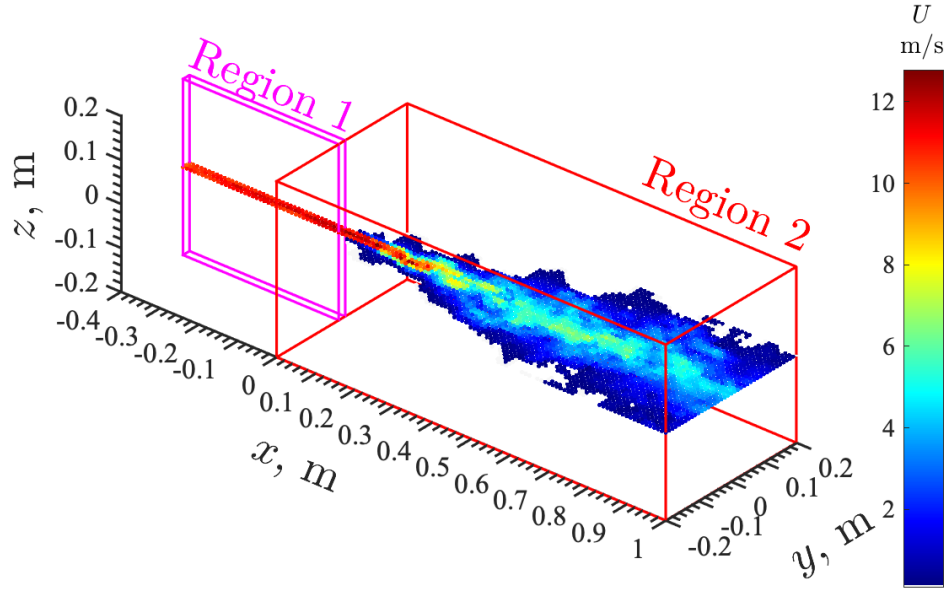


Figure 1: Computational configuration in the planar jet simulation with the contour plot of instantaneous streamwise at $z = 0$

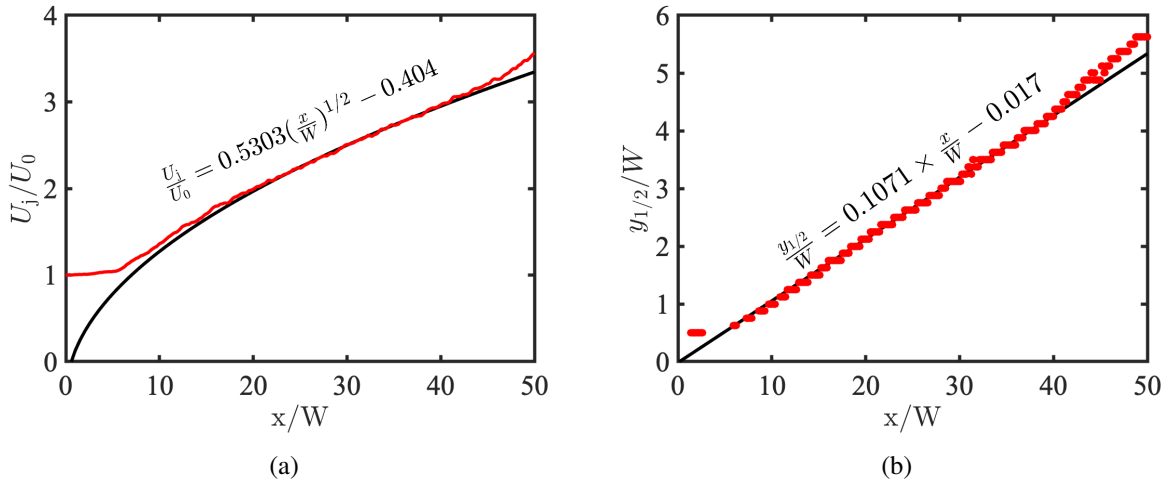


Figure 2: Planar jet (a) normalized mean centerline streamwise velocity U_j/U_0 and (b) scatter data of normalized jet half-width $y_{1/2}/W$ values. Curve fits computed for data within range: $20 \leq x/W \leq 40$

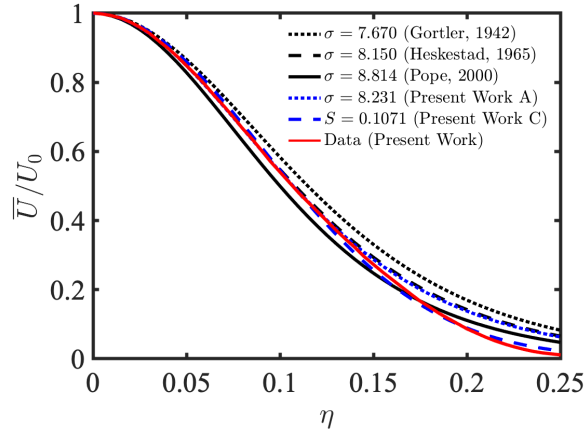


Figure 3: Planar jet normalized mean streamwise velocity \bar{U}/U_0 profile

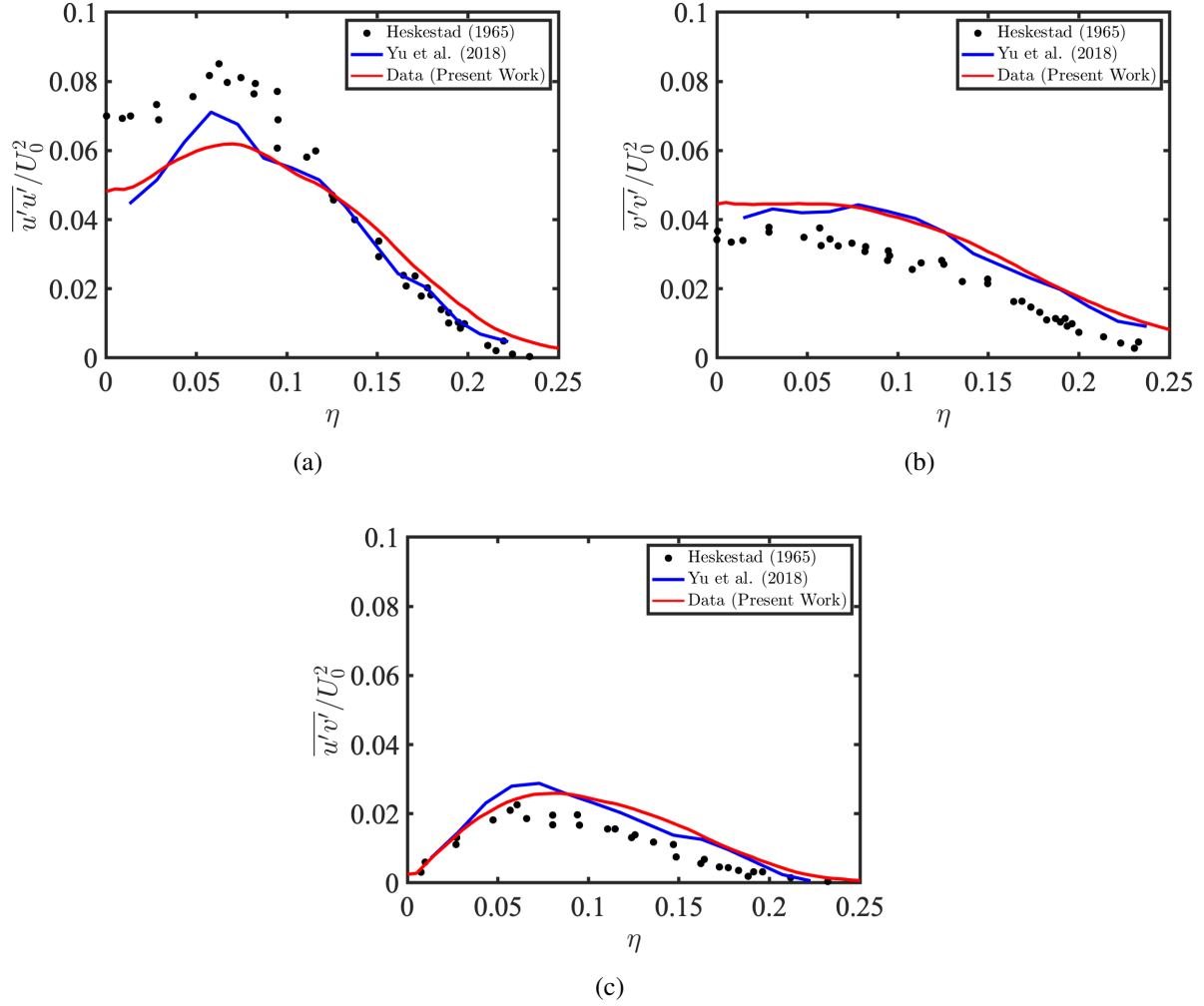


Figure 4: Planar jet dimensionless Reynolds stresses; (a) $\overline{u'u'}/U_0^2$; (b) $\overline{v'v'}/U_0^2$; and (c) $\overline{u'v'}/U_0^2$.

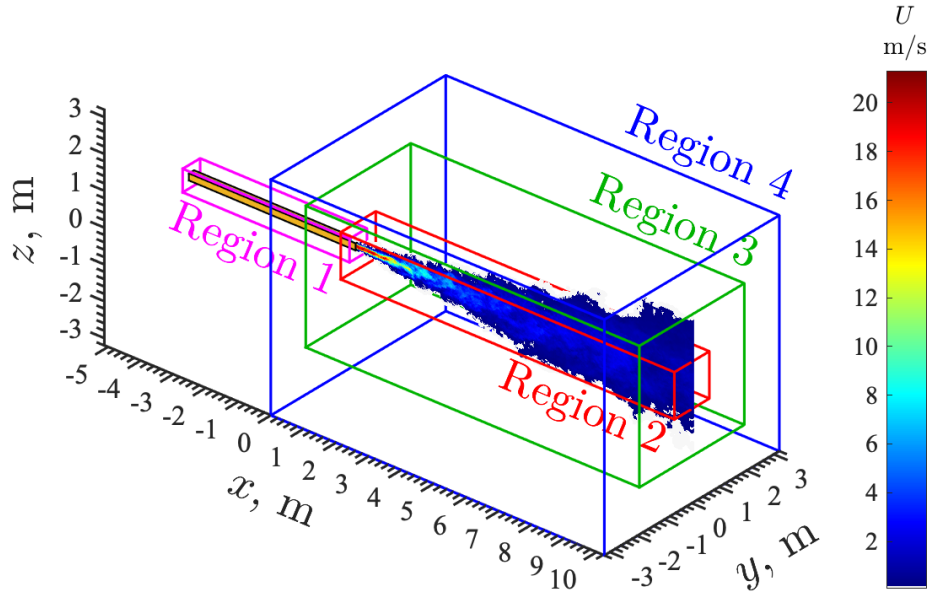


Figure 5: Computational configuration in the round jet simulation with the contour plot of instantaneous streamwise at $y = 0$

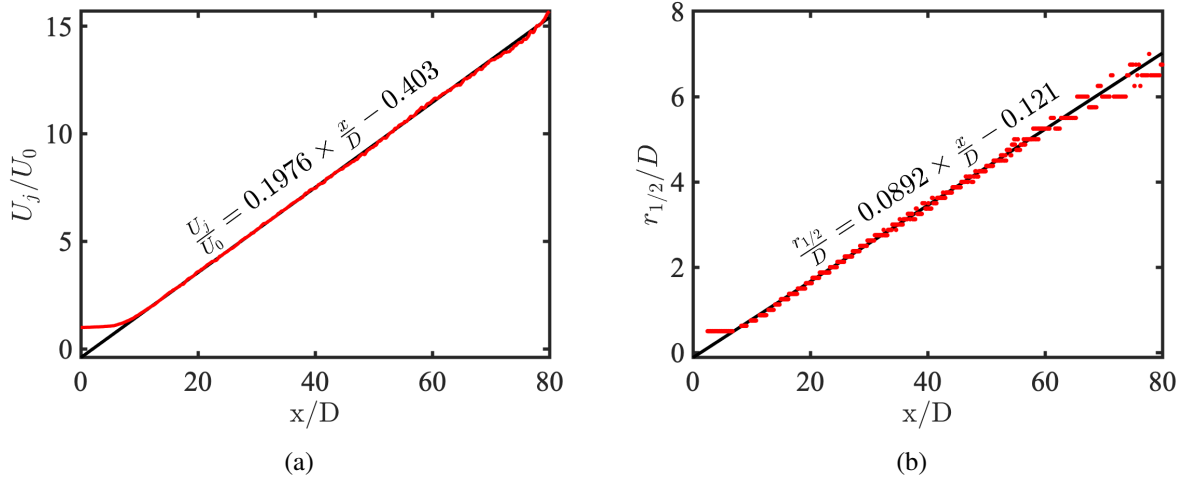


Figure 6: Round jet (a) normalized mean centerline streamwise velocity U_j/U_0 and (b) scatter data of normalized jet half-width $r_{1/2}/D$ values. Linear curve fits computed for data within range: $20 \leq x/D \leq 60$

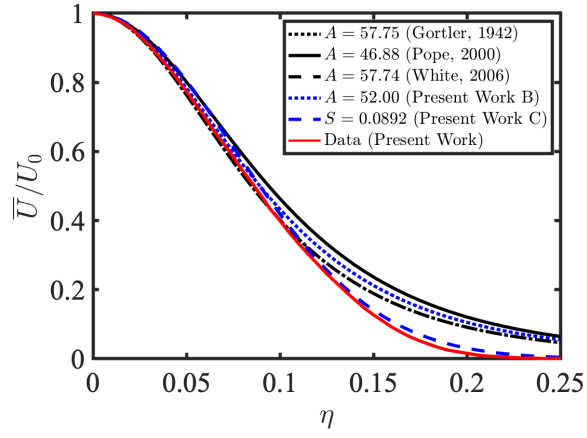


Figure 7: Round jet normalized mean streamwise velocity \bar{U}/U_0 profile

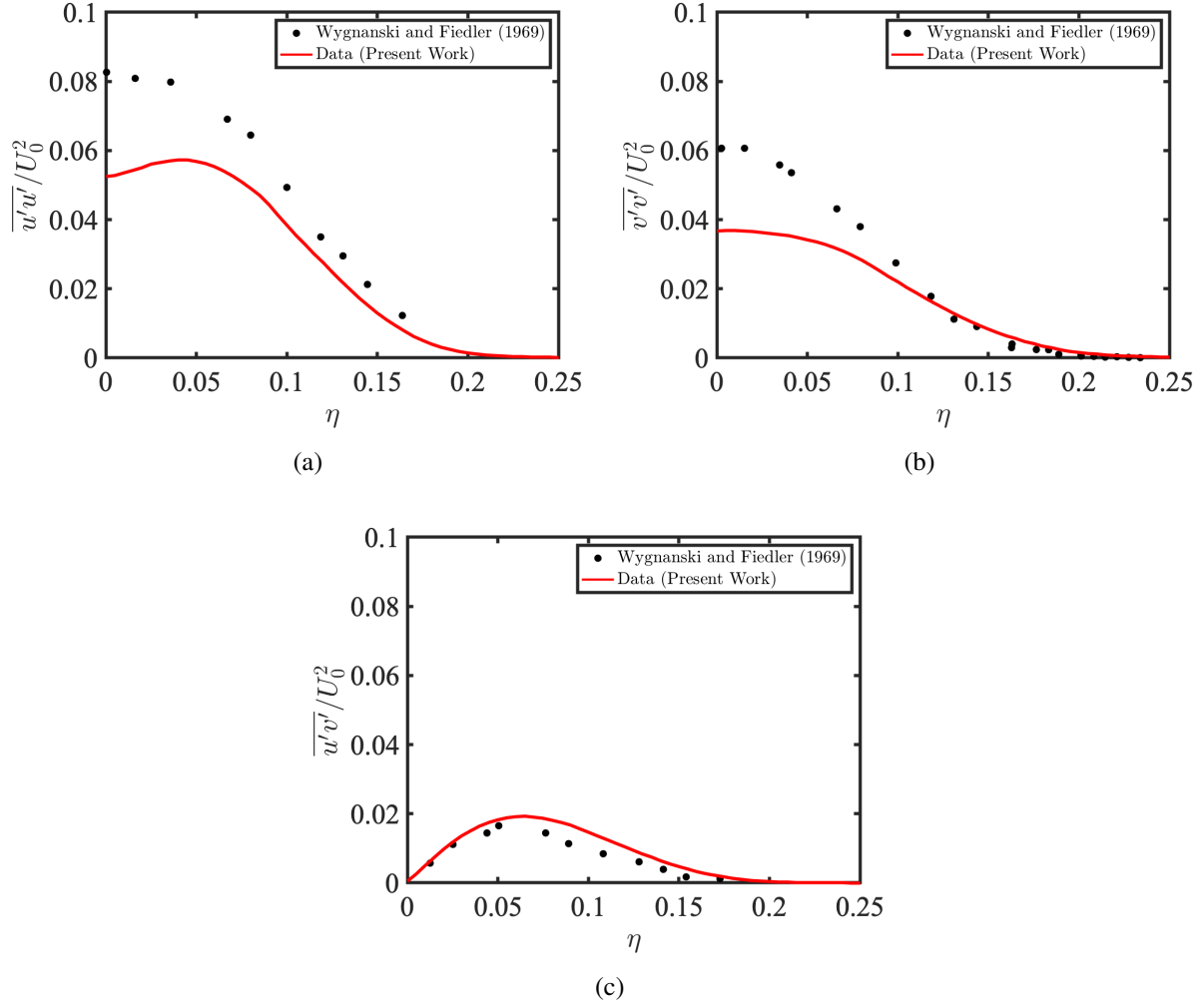


Figure 8: Round jet dimensionless Reynolds stresses; (a) $\overline{u'u'}/U_0^2$; (b) $\overline{v'v'}/U_0^2$; and (c) $\overline{u'v'}/U_0^2$.

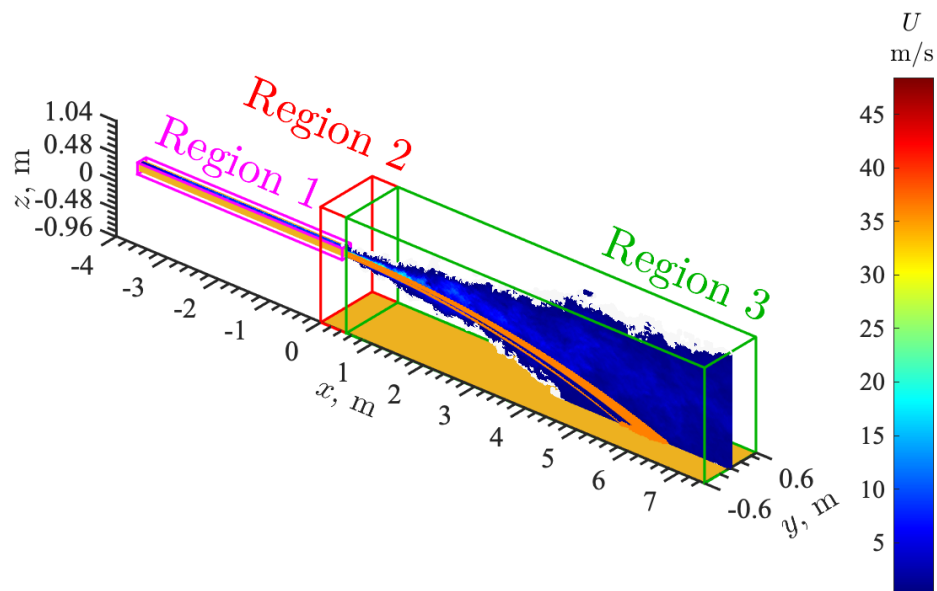


Figure 9: Computational configuration with the contour plot of instantaneous streamwise velocity at $y = 0$ and firebrand trajectories.

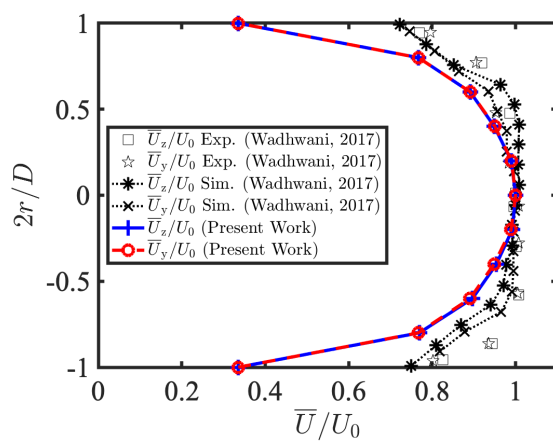


Figure 10: Dimensionless mean velocity profile at the jet exit in the firebrand deposition simulation

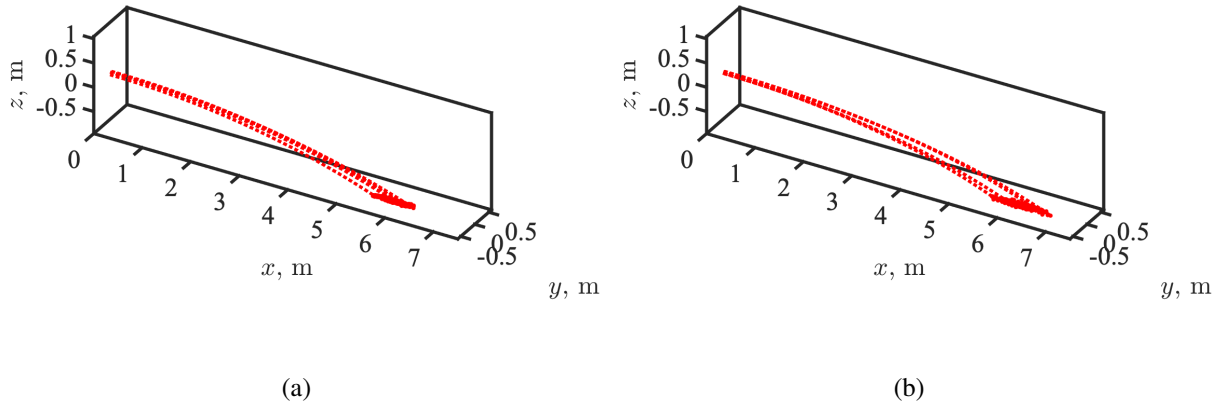


Figure 11: Firebrand trajectories with deposited firebrands; (a) cubiform; and (b) cylindrical firebrands.

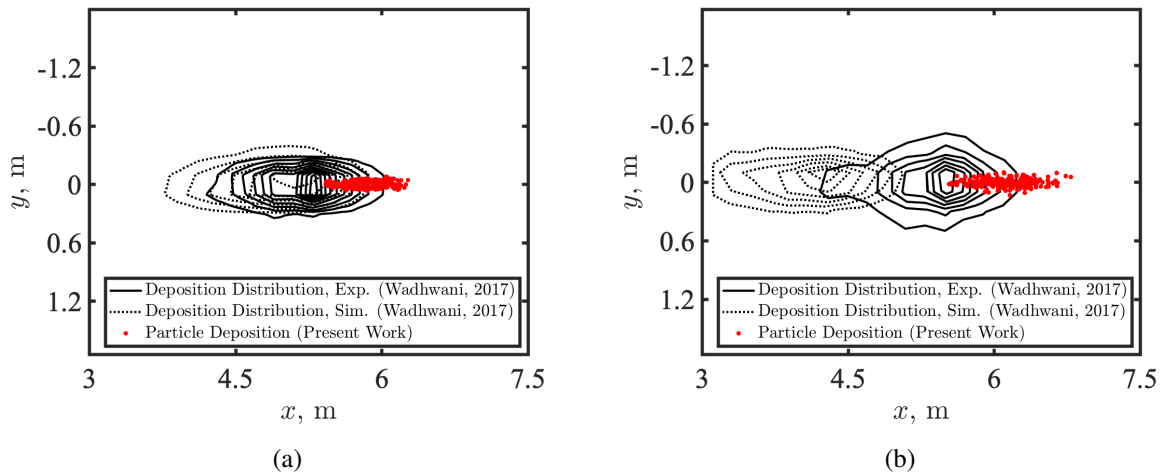


Figure 12: Firebrand deposition patterns for (a) cubiform and (b) cylindrical firebrand simulations